

# Electroluminescence analysis of silicon interdigitated back contact solar cells with a front surface selective band offset barrier

Koffi F. Ahanogbe<sup>1,2,\*</sup> , José Alvarez<sup>1,2</sup>, Alexandre Jaffré<sup>1,2</sup>, James P. Connolly<sup>1,2</sup>, Marie-Estelle Gueunier-Farret<sup>1,2</sup>, Erwann Fourmond<sup>3</sup> , Seif El-Whibi<sup>3</sup>, Alain Fave<sup>3</sup> , Perrine Carroy<sup>5</sup> , Zakaria Djebbour<sup>1,2,4</sup>, and Jean-Paul Kleider<sup>1,2</sup> 

<sup>1</sup> Université Paris-Saclay, CentraleSupélec, CNRS, Laboratoire de Génie Electrique et Electronique de Paris, 91192 Gif-sur-Yvette, France

<sup>2</sup> Sorbonne Université, CNRS, Laboratoire de Génie Electrique et Electronique de Paris, 75252 Paris, France

<sup>3</sup> Univ. Lyon, INSA Lyon, CNRS, Ecole Centrale de Lyon, Université Claude Bernard Lyon 1, CPE Lyon, INL, UMR5270, 69621 Villeurbanne, France

<sup>4</sup> Département des Sciences Physiques, UVSQ, Université Paris-Saclay, 45 Av. des États-Unis, 78035 Versailles cedex, France

<sup>5</sup> CEA, LITEN, INES, Department of Solar Technologies, 73375 Le Bourget du Lac, France

Received: 1 February 2022 / Accepted: 13 June 2022

**Abstract.** Electroluminescence allows rapid characterization of an entire photovoltaic solar cell and visualization of defects at the micrometer scale. Here we focus on the optoelectronic properties of silicon interdigitated back contact cells characterized by electroluminescence. The spatially resolved electroluminescence helps us control the quality of interdigitated back contact structures used in silicon bottom subcells in a three-terminal tandem perovskite on silicon solar cell. Local variations in minority carrier diffusion length, surface recombination velocity and, the impact of resistive and optical losses were analyzed by electroluminescence mapping. In addition, we quantify the radiative saturation current density and the radiative open circuit voltage using the electroluminescence spectrum of the cell. This step allows us to accurately assess the performance limits induced in the device due to the non-radiative recombination.

**Keywords:** Electroluminescence / characterization / three-terminal / tandem solar cell

## 1 Introduction

The development of a new generation of multijunction solar cells based on wide bandgap materials, holds excellent potential for high efficiency photovoltaics. The materials combination in tandem devices such as perovskite on silicon requires a good knowledge of the optoelectronic properties of each junction. In the literature, there are a number of characterization techniques based on solar cell luminescence, such as electroluminescence (EL). EL technique [1] provides very rich information on solar cell devices from both imaging and spectral analysis [1–5] EL imaging which is complementary to photoluminescence (PL) is a spatially resolved characterization tool for silicon solar cells [6] and silicon modules [7]. The EL image contains cell quality information and electronic properties, including properties related to the

recombination of carriers such as carrier diffusion length [8] and surface recombination velocity. For advanced quantitative analysis, the spectrally resolved EL is useful to provide additional electrical properties of the sample and its performance limit since the energies of the emitted photons are close to the bandgap [9].

The purpose of this work is to analyze the N-type silicon interdigitated back contact solar cells (Si-IBCs) using the EL technique. The samples considered here are chosen as bottom subcells to develop a proof of concept of three-terminal selective band offset barrier (3T-SBOB) perovskite on silicon tandem solar cell [10–17].

After a brief overview of EL theory, we first present the results of characterization of two Si-IBCs, and four passivated Si-IBCs with intrinsic and doped amorphous silicon layers based on spatially resolved EL analysis for fast quality control. In addition, we have performed a quantitative analysis of Si-IBC performance limits using coupled spectral electroluminescence and quantum efficiency analysis.

\* e-mail: [koffi.ahanogbe@centralesupelec.fr](mailto:koffi.ahanogbe@centralesupelec.fr)

## 2 Electroluminescence theory

The Shockley-Queisser (SQ) approach [18] used to calculate the efficiency limit of a single junction solar cell is based on the principle of the detailed balance between absorption and emission of light. This principle requires that absorption is only possible when emission of photons is also allowed [19]. If we assume that the quasi-Fermi level splitting  $\Delta E_f$  is constant over the thickness of the device, the luminescent flux is:

$$\varphi_{em}(E) = a(E) \times \varphi_{gb}(E) \times \left[ \exp\left(\frac{\Delta E_f}{k_B T}\right) - 1 \right], \quad (1)$$

where  $k_B$  is the Boltzmann constant,  $T$  the absolute temperature,  $a(E)$  the absorptance and  $\varphi_{gb}(E)$  the photon spectral density described with general Planck's law of grey body at  $T$ , as:

$$\varphi_{gb}(E) = \frac{2\pi E^2}{h^3 c^2 \left[ \exp\left(\frac{E}{k_B T}\right) - 1 \right]} \approx \frac{2\pi E^2}{h^3 c^2} \times \exp\left(-\frac{E}{k_B T}\right), \quad (2)$$

$h$  being Planck's constant and  $c$  the speed of the light in vacuum.

The quasi-Fermi level splitting changes within the absorber volume for a real solar cell. That makes the calculation of the luminescence complex. Nevertheless, the SQ approach can be generalized by the optoelectronic reciprocity relation reported by Rau [20]. Under the assumptions that the charge transport in a solar cell is by diffusion rather than by drift and that recombination is linear in minority carrier concentration [20], the local electroluminescence emission at any position  $\vec{r}$  of the cell is given by

$$\varphi_{em}(E, \vec{r}) = Q_e(E, \vec{r}) \varphi_{gb}(E, \vec{r}) \times \left[ \exp\left(\frac{qV(\vec{r})}{k_B T}\right) - 1 \right], \quad (3)$$

where  $V(\vec{r})$  is the local internal voltage defined as the quasi-Fermi level splitting at the edge of space-charge region and  $Q_e(E, \vec{r})$  the photovoltaic external quantum efficiency. Equation (3) follows from equation (1) for lossless photo-generated carrier collection, such that quantum efficiency is equal to absorptance  $a(E)$  (in particular if carrier mobilities are sufficiently high). If  $a(E)$  is a step function of 1 above the bandgap to 0 below, we quickly recover the original SQ approach [21]. Furthermore, most of the physical processes in photovoltaics are described by equation (3) [20].

The external quantum efficiency  $Q_e(E, \vec{r})$  expresses the recombination and optical losses, while the internal voltage  $V(\vec{r})$  reflects the resistive losses. For next macroscopic analysis (spectral analysis for example) we assume that  $Q_e(E, \vec{r})$  and  $V(\vec{r})$  are almost spatially independent and thus equal to  $Q_e(E)$  and  $V$  respectively.

### 2.1 Radiative recombination current

We will analyze the radiative limit of our cells in Section 4.3 using external quantum efficiency. The dark current density of the solar cell can be defined using equation (3) as:

$$J_d = q \int_0^\infty Q_e(E) \varphi_{gb}(E) \times \left[ \exp\left(\frac{qV}{k_B T}\right) - 1 \right] dE, \quad (4)$$

where  $q$  is the elementary charge.

From equation (4), we define  $J_{0,rad}$  as:

$$J_{0,rad} = q \int_0^\infty Q_e(E) \varphi_{gb}(E) dE, \quad (5)$$

$J_{0,rad}$  represents the lower limit of emitted photons close to the band edge called radiative saturation current density. Note that  $J_{0,rad}$  becomes the SQ limit

$$J_{0,SQ} = q \int_{E_g}^\infty \varphi_{gb}(E) dE, \quad (6)$$

when replacing the  $Q_e(E)$  by a step function.

Furthermore, the total current density under illumination follows as

$$J = J_{0,rad} \left[ \exp\left(\frac{qV}{k_B T}\right) - 1 \right] - J_{sc}, \quad (7)$$

with

$$J_{sc} = q \int_0^\infty Q_e(E) \varphi_{sun}(E) dE, \quad (8)$$

and SQ limit introducing the step function for  $Q_e(E)$ :

$$J_{sc,SQ} = q \int_{E_g}^\infty \varphi_{sun}(E) dE. \quad (9)$$

### 2.2 Limit of the open circuit voltage

From equation (7) we obtain the radiative limit of the open circuit voltage

$$V_{oc,rad} = \frac{k_B T}{q} \ln\left(\frac{J_{sc}}{J_{0,rad}} + 1\right), \quad (10)$$

with  $J_{0,rad}$  given by equation (5). This represents the upper limit of open circuit voltage that can be achieved by the solar cell. Increasing non-radiative recombination in the cell increases the saturation current and decreases the measured open circuit voltage  $V_{oc}$ . We can therefore define and quantify the contribution of non-radiative recombination losses as

$$\Delta V_{oc,nrad} = V_{oc,rad} - V_{oc}. \quad (11)$$

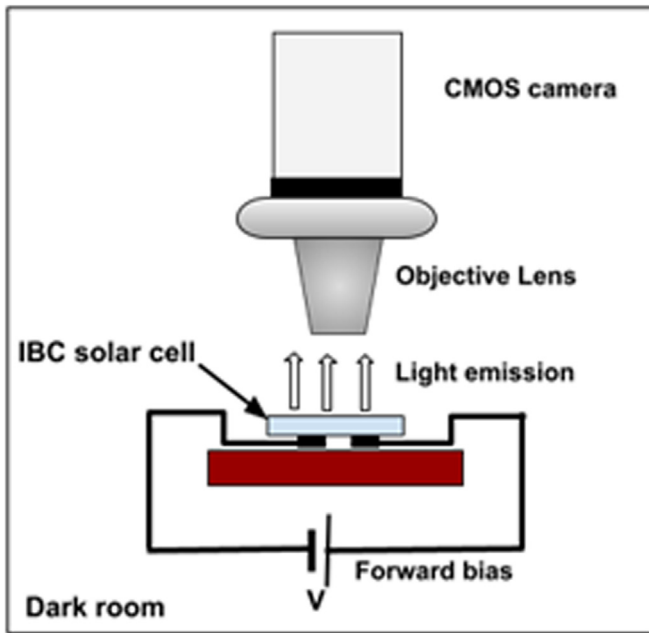


Fig. 1. Schematic of EL setup.

### 3 Experimental

#### 3.1 EL imaging bench

The spatially resolved EL characterization technique uses a photon detector to capture light emitted by a sample that luminesces under an applied forward bias. Figure 1 shows a schematic of the EL setup.

All measurements are performed in dark conditions at constant temperature of 298 K using a silicon CMOS image sensor. The photon detector is an uncooled Sony IMX174 monochrome chip. Light is collected with a digital single-lens reflex of 50 mm focal length at  $f/1.4$  aperture. We measured a sampling ratio of  $25 \mu\text{m}/\text{pixel}$  using an imaging target. For each measurement, we acquired 10 EL images and 10 dark images of the sensor. To increase the signal-to-noise ratio, we stacked the 10 EL images and removed the CMOS dark images using Autostakkert software. Finally, the EL mapping obtained after data processing (using ImageJ and Gimp software) corresponds to the emission from radiative recombination within the sample. The average spectrum of the solar cell is obtained by the same bench replacing the CMOS camera with a confocal microscope ( $\mu\text{-PL}$ ) described below.

#### 3.2 Confocal microscopy setup

EL spectrum and  $\mu\text{-PL}$  measurements were performed on a WiTec alpha-300R confocal microscope in a backscattering configuration. After cell polarization (EL case), the signal is collected through the same objective and guided to the Princeton SP-2300 spectrometer with a  $200 \mu\text{m}$  core optical fiber. The detector is an Andor DU491A with a 124 pixels CCD array cooled to  $-70^\circ\text{C}$ . The grating used is blazed at 1200 nm and is 150 grooves/mm, leading to a spectral resolution of 3 nm. The CCD dark spectra have

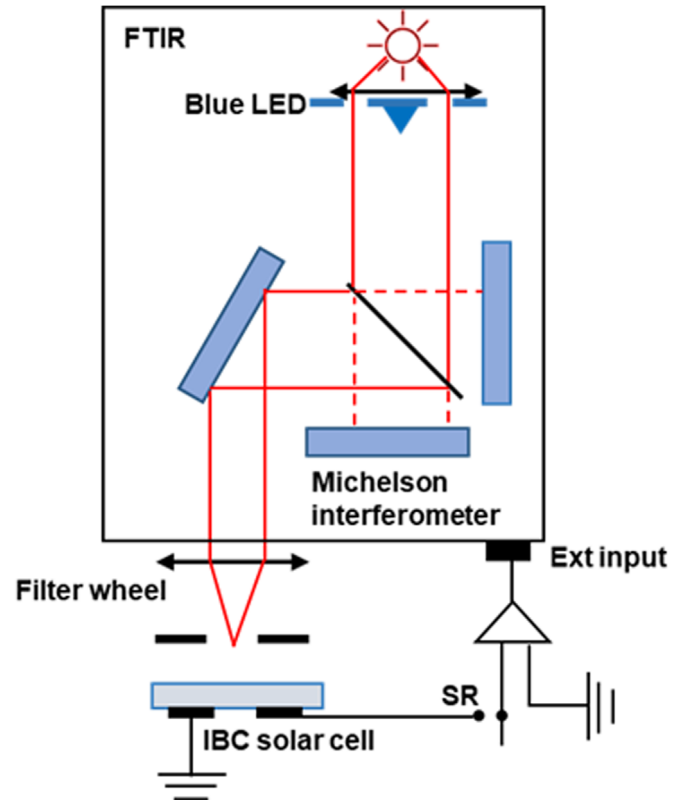
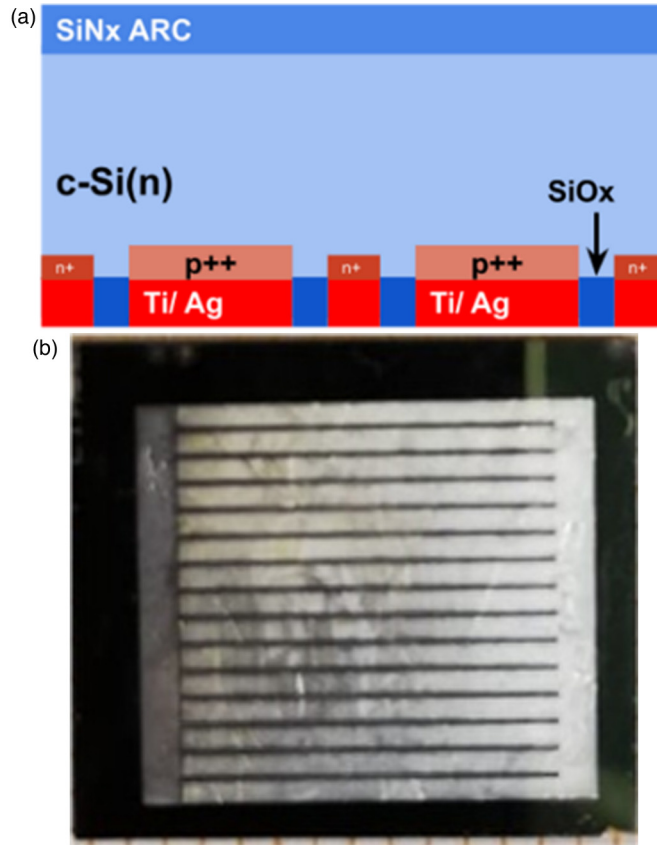


Fig. 2. Schematic of the designed setup for spectral response and quantum efficiency measurements. Light outgoing from FTIR is focused on the IBC cell via an optical fiber. The cell photocurrent is amplified by the current voltage converter and re-injected as external input into the FTIR and transformed to the cell spectra. Note that this setup allows reflection-transmission measurements and FTPS-Fourier Transform Photocurrent Spectroscopy acquisition.

been removed from each spectrum. The  $\mu\text{-PL}$  setup has the same detection configuration, and samples were excited at 532 nm through an Olympus  $20\times$  long working objective, with 6.5 mW laser power ( $82 \mu\text{W}/\mu\text{m}^2$ ). The  $\mu\text{-PL}$  mapping was performed using the XY stepper stage of the microscope, with a  $100 \mu\text{m}$  spacing between each point for EL and PL. The spatial resolution is, therefore,  $100 \mu\text{m}$ .

#### 3.3 Quantum efficiency measurement

We used a Nicolet IS50R Fourier transform infrared spectrometer (FTIR) from Thermo Scientific to measure the spectral response (SR) and then deduced external quantum efficiency  $Q_e(E)$ . The beam split of the interferometer inside the FTIR is a quartz plate that enables us to work from 390 nm to 1800 nm wavelength range. Figure 2 shows the setup developed around the spectrometer that allows performing  $Q_e(E)$  measurements [22]. The light coming from the FTIR is a combination of halogen lamp and LEDs (emitting in the UV, green and blue) and is directed on the cell via a fiber. The photocurrent generated by the cell is amplified by a high gain current/voltage converter (DLPCA-200 from FEMTO) before being re-injected into the FTIR to be processed and, hence, obtain the corresponding spectra.



**Fig. 3.** Schematic (a) and back side image (b) of the silicon interdigitated back contact solar cell.

## 4 EL characterization results

### 4.1 EL imaging on silicon IBC

In this section, we present a description of the IBC devices without SBOB layers, and we discuss their EL and PL maps. Two solar cells labeled Si-IBC-1 and Si-IBC-2, both of  $1 \text{ cm}^2$  area, were used (Fig. 3). These samples are fabricated from an n-type float zone silicon wafer ( $270 \mu\text{m}$ ) with a resistivity of  $\rho = 3 \Omega\text{cm}$ . The emitter is formed by boron ion implantation and the n++ contact by high-temperature phosphorus diffusion ( $900^\circ\text{C}$ ).

The front surface is flat and covered by a hydrogenated silicon nitride  $\text{SiN}_x\text{:H}$  stack deposited by plasma-enhanced CVD (PECVD). First layer is 10 nm Silicon-rich  $\text{SiN}_x\text{:H}$  for surface passivation, followed by 70 nm of standard  $\text{SiN}_x\text{:H}$  for anti-reflective coating (ARC). They have open-circuit voltages of  $V_{oc,1} = 560 \text{ mV}$  and  $V_{oc,2} = 580 \text{ mV}$ , and efficiencies of  $\eta_1 = 11.47\%$  and  $\eta_2 = 13.8\%$ , respectively under AM1.5 G illumination. Note that the Si-IBC-2 current density is higher than the Si-IBC-1. It explains the difference between the cell efficiencies.

Figure 4 shows the EL image (Fig. 4a) at 0.9 V compared to the PL image (Fig. 4b) of Si-IBC-1. The EL image is obtained in less than 15 minutes whereas PL images require six hours of data acquisition.

Light emission (PL and EL) by the sample is quite homogeneous but we can distinguish a defect zone where the emission intensity is reduced on the top right. This result is confirmed by spectral response measurements (not shown here). The high defect zone is accurately identified on the EL image (by the dashed circle) and on the PL picture.

The EL and PL corresponding images of the Si-IBC-2 are shown in Figure 5a and b respectively. The PL image is homogeneous with no visible surface defect zone. We note three different zones with dark (bottom left), bright (top right) and high intensity spots (white circles) on EL image. The Si-IBC-2 sample is less luminescent compared to the Si-IBC-1 due to the impact of resistive losses and local variation of the electronic properties.

As mentioned above (in Sect. 2), all physical processes appear and impact the radiative emission as described by equation (3). The first factor  $Q_e(E, \vec{r})$  gives information on recombination and optical losses. The reflectance of the two samples was performed and results show no difference in shapes. As we apply forward bias, the EL emission of both samples is strongly affected by resistive losses.

Figure 6 shows the EL images of the Si-IBC-1 (Fig. 6a) and Si-IBC-2 (Fig. 6b) when 0.6 V is applied. This value corresponds to an injection current of 10 mA. Since resistive losses occur at higher voltage, these images are less impacted by the resistive losses because of the low current injected.

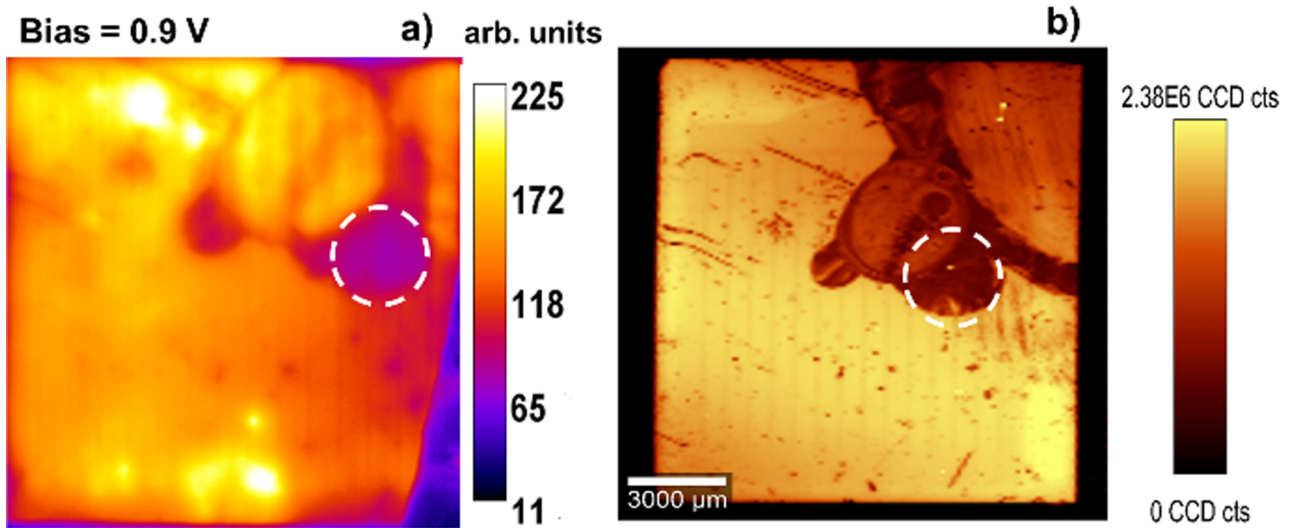


**Fig. 4.** (a) EL image of Si-IBC-1 at 0.9 V bias compared to (b) PL image obtained by  $\mu$ -confocal microscope, excitation wavelength is 532 nm. The white circle indicates the high electrical defect zone.

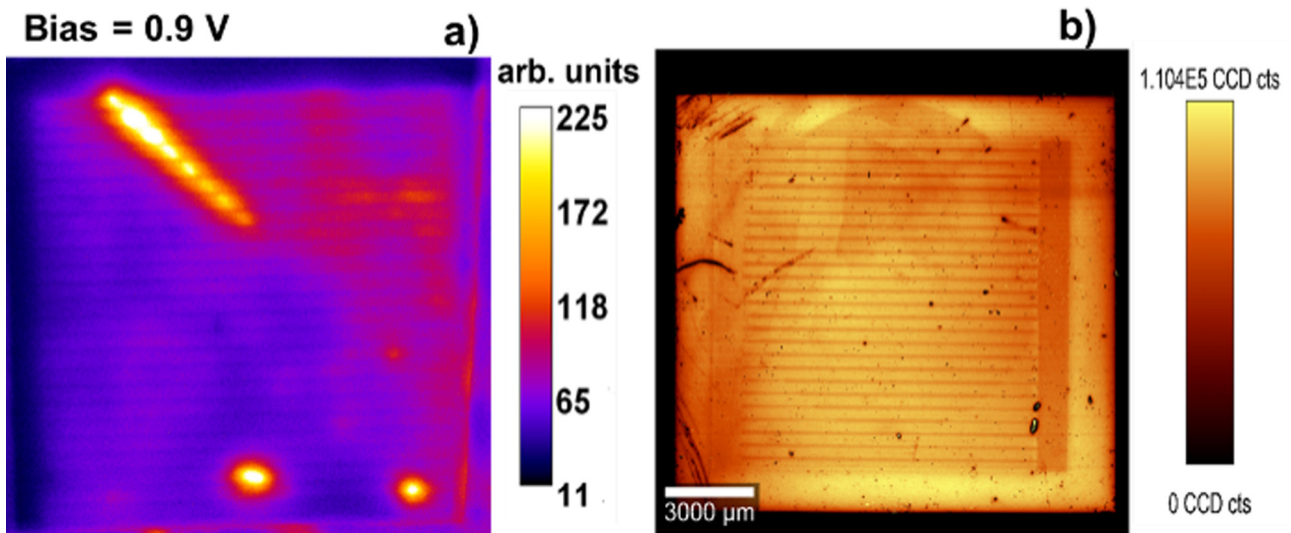


**Fig. 5.** (a) EL image of Si-IBC-2 at 0.9 V bias compared to PL image (b) obtained by  $\mu$ -confocal microscope.

Comparing the EL images at different biases for Si-IBC-1 (Figs. 4a to 6a) and Si-IBC-2 (Figs. 4b to 6b), we observe that the resistive losses more impact the Si-IBC-2. Elsewhere, the local variation of the intensity in Figure 5 is linked to the local variation of the optoelectronic properties. Indeed, the high minority carrier diffusion length zone is characterized by the high EL intensity. In particular, the very bright spots on the Si-IBC-2 EL image correspond to places where the recombination surface velocity is locally very low.

#### 4.2 EL imaging on bottom cells for 3T devices

In this section, we present a description of four IBC samples with SBOB layers, and we focus on their EL maps. Due to its attractiveness and swiftness, we used the EL technique to characterize four Si-IBC bottom cells prepared for three-terminal tandem fabrication labeled A, B, C, and D.

All bottom subcells have the conventional previously described IBC configuration, and the front surface is passivated with a stack of thin intrinsic and doped hydrogenated amorphous silicon layers (5 nm each) and covered with a 12 nm thick Indium Tin Oxide (ITO) layer, as depicted in Figure 7.

The EL images of the four samples are presented in Figure 8. First, we note the difference between radiative emission intensity which is higher for samples A and B than for C and D.

Note that all measurements have been performed in the same conditions with 1 V voltage bias. Samples C and D are show lower EL intensity in these condition because of higher non-radiative recombination. Note that the lifetime measurements were performed using the microwave-detected photoconductance decay ( $\mu$ W-PCD) technique and show low effective carrier lifetime of around 38  $\mu$ s. Therefore, we conclude that non-radiative recombination is

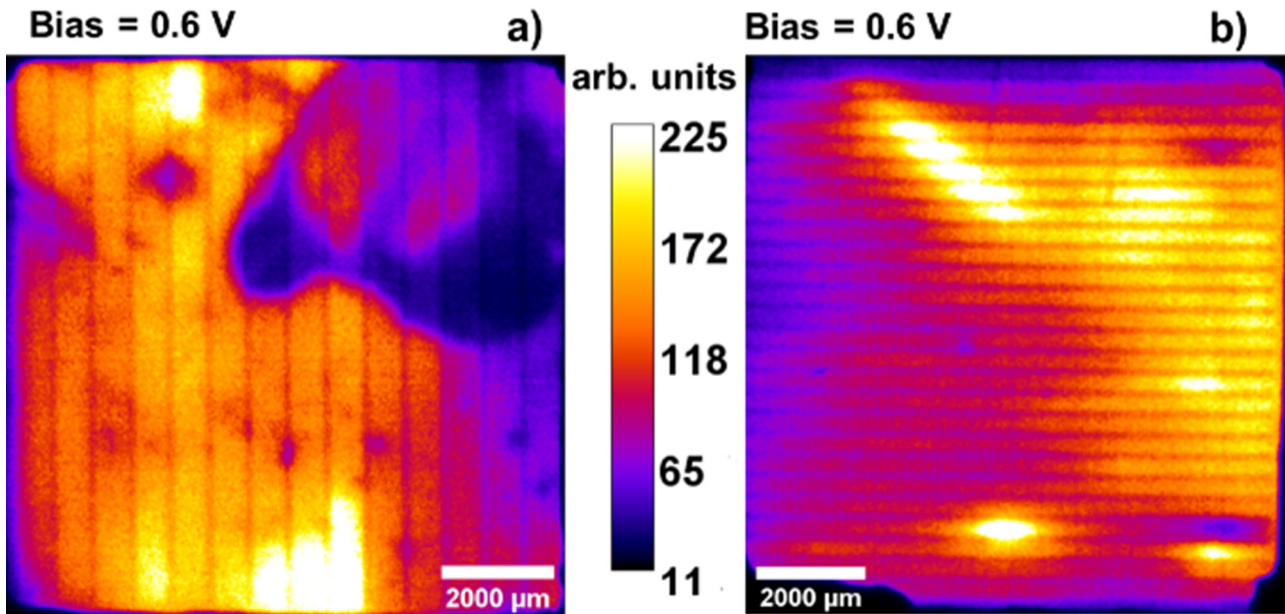


**Fig. 6.** EL image of Si-IBC-1 (a) and Si-IBC-2 (b) at 0.6 V bias corresponding to low injection (10 mA) current operating mode.

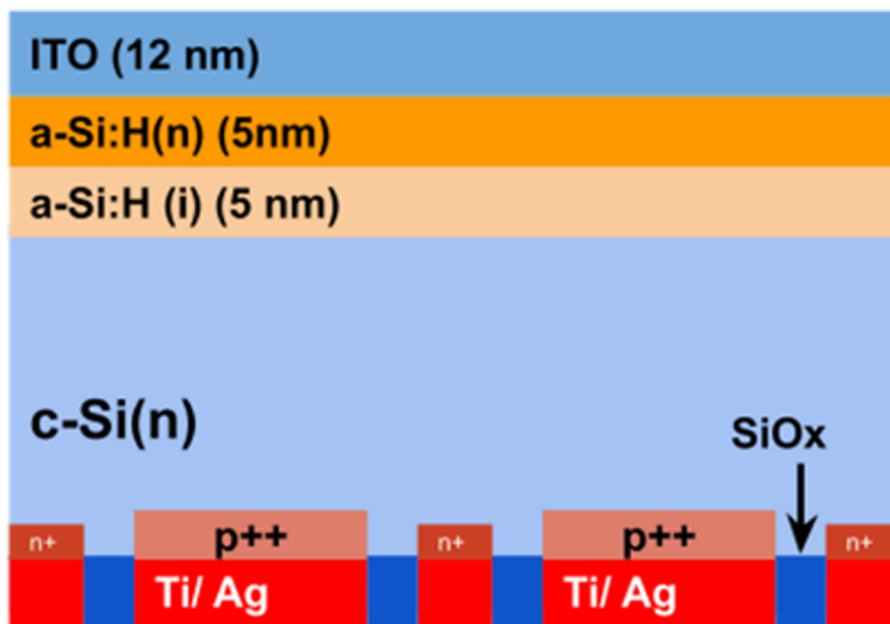


**Fig. 7.** Architecture of the Si-IBC bottom subcells. It is a conventional Si-IBC solar cell with the top surface passivated by a stack of thin intrinsic and doped hydrogenated amorphous silicon layers and covered with ITO.

dominated mostly by the surface recombination. In addition, we observed horizontal dark lines (shown by black arrows on Fig. 8) on the images of samples B, C, and D. These dark lines are due to a poor adherence of the fingers and a poor metallization.

Furthermore, the samples C and D have less shunt resistance confirmed by the dark current-voltage curve presented in Figure 9. Finally, their photovoltaic performance (not presented here) is low.

This shows that EL imaging is thus a fast, suitable, and practical technique to control the device's state.

### 4.3 Performance limit analysis of Si-IBC-2

Here we present the performance limit of the Si-IBC-2 and quantify its radiative and non-radiative recombination. We chose this sample because it has fewer defects, and its electroluminescence spectrum shows a good signal-to-noise ratio. When measuring the EL, we have applied a bias of 1.1 V to generate the signal. We have measured the quantum efficiency with FTIR in short-circuit conditions. In general, the external quantum efficiency  $Q_e(E)$  measurement contains information on optical properties and

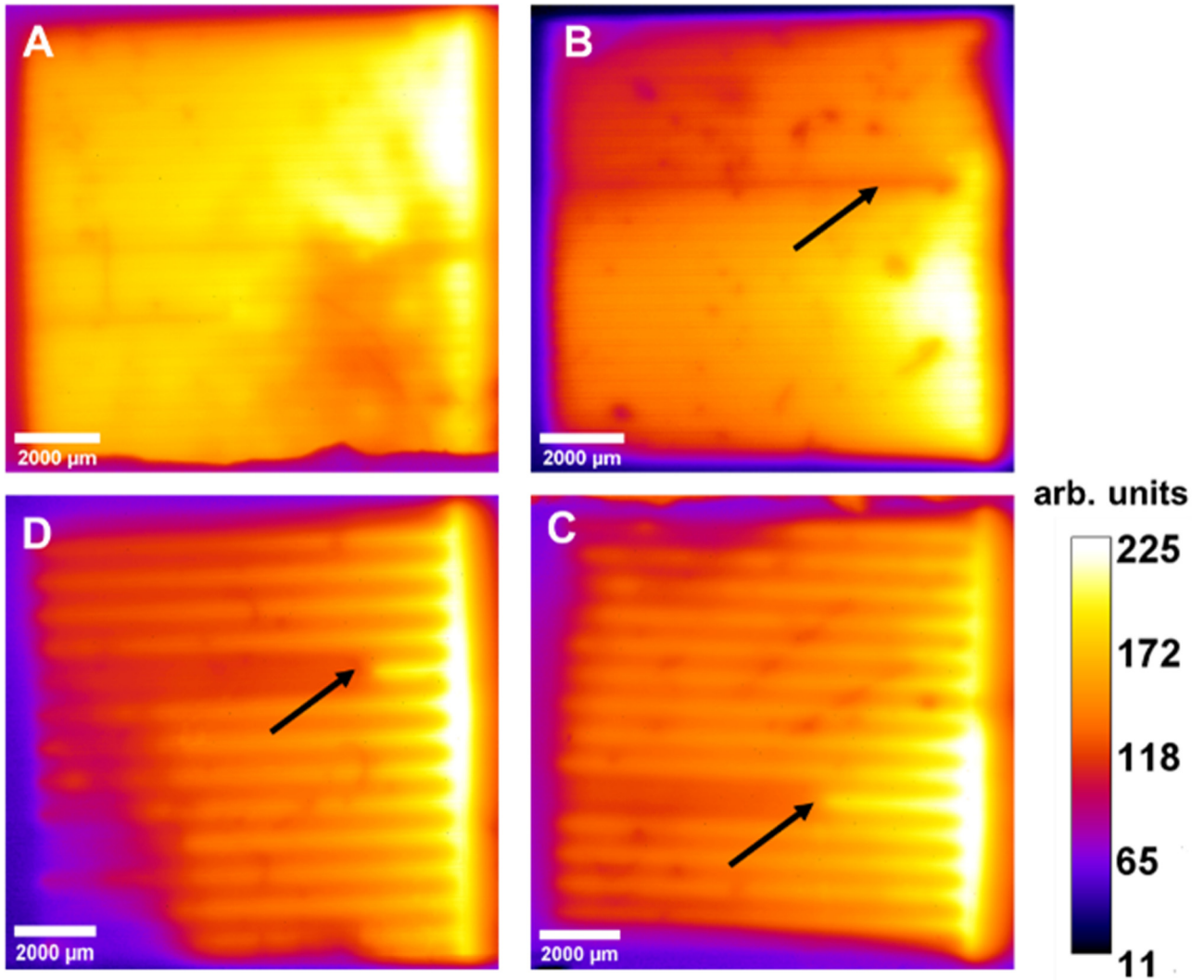


**Fig. 8.** EL image of four different 3T-bottom cells, labelled A, B, C, and D, under 1 V applied bias. EL intensity is two times greater in samples A and B than C and D due to the non-radiative recombination. Dark arrows indicate a lousy adherence of fingers.

recombination behavior of the solar cell. According to equation (3), the EL spectrum contains in principle the same information as the  $Q_e(E)$  spectrum and the weighting factor in the reciprocity relation depends exponentially on photon energy ( $\varphi_{gb}$ ). Since all higher energies  $E$  are damped by  $\exp\left(-\frac{E}{k_B T}\right)$ , EL is only measurable close to the bandgap.

Figure 10 shows the directly measured  $Q_e\_dir$  curve (with the FTIR setup) [22] and the EL spectrum (obtained by a confocal microscope (red Lorentzian curve).

The EL spectrum is characterized by a broad peak around 1.12 eV which corresponds to the Si indirect bandgap.

The  $Q_e\_EL$  data set in Figure 10 corresponds to the quantum efficiencies that are obtained by scaling the EL spectrum according to equations (3) and (4). As we can see, the  $Q_e\_EL$  fits partially well with  $Q_e\_dir$ , within the lower energy part until 1.25 eV and both data show a relatively small transition between low and high quantum efficiency. Therefore, we can say that the absorber has a good crystallinity [23].

We are now able to calculate the radiative saturation current density  $J_{0,rad}$  defined by the equation (5) using the  $Q_e\_EL$ . With this value, one can deduce the radiative open circuit voltage  $V_{oc,rad}$  (using Eq. (10)) and the measured short circuit current  $J_{sc}$ .

Table 1 presents a comparison between our Si-IBC-2 solar cell performance and a high quality 2T terminal silicon solar cell [23]. The extracted  $J_{0,SQ}$  and  $J_{0,rad}$  are higher in our Si-IBC-2 cell than in the reference.  $J_{0,rad}$  and  $V_{oc,rad}$  are equal to  $1.77 \times 10^{-15}$  mA/cm<sup>2</sup> and 797 mV respectively. By comparing  $V_{oc,rad}$  with the open circuit voltage  $V_{oc}$  (580 mV) derived from the  $J-V$  curve (performed under illumination AM1.5G not presented here), we deduce the difference  $\Delta V_{oc,nrad} = 217$  mV that defines the contribution of the non-radiative recombination to the saturation current density that consequently decreases the open circuit voltage. Note that the losses in short-circuit density are neglected here. Obviously, this value is relatively high because of the high ratio  $\Delta V_{oc,nrad}/V_{oc,rad}$  (non-radiative to radiative recombination) shown in Table 1. In the case of high-quality passivated surfaces

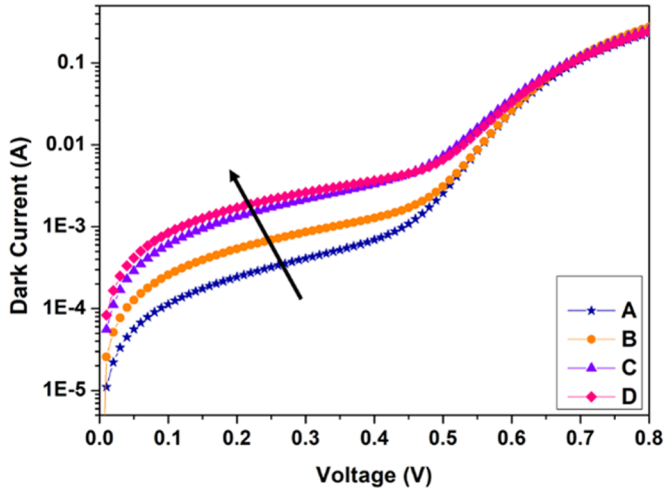


**Fig. 9.** Semilogarithmic plots of dark  $IV$  curves of bottom cells A, B, C, and D for 3T devices. The black arrow indicates the direction of decrease of the shunt resistance. The samples C and D have then less shunt resistance ( $152 \Omega\text{cm}^2$  and  $118 \Omega\text{cm}^2$ ) than the samples A and B ( $827.6 \Omega\text{cm}^2$  and  $372.5 \Omega\text{cm}^2$  respectively). Shunt Resistance value is obtained by a two-diode fit model).

**Table 1.** Si-IBC (2) external photovoltaic parameters calculated as specified in the theory section, compared with 2T Silicon device parameters from Kirchartz et al. [23]. SQ-values under AM1.5G illumination saturation current density  $J_{0,SQ}$ , short circuit current density  $J_{sc,SQ}$  and open circuit voltage  $V_{oc,SQ}$  are compared the spectral responded values  $J_{sc}$ ,  $V_{oc}$  and to the EL and EQE analysis parameters  $J_{0,rad}$ ,  $V_{oc,rad}$ .

	Si-IBC (2)	Si (2T) Ref. [23]
$E_g$ (eV)	1.12	1.12
$J_{0,SQ}$ (A/cm <sup>2</sup> )	$1.05 \times 10^{-16}$	$8.2 \times 10^{-17}$
$J_{sc,SQ}$ (mA/cm <sup>2</sup> )	43.4	43.4
$V_{oc,SQ}$ (mV)	875	876
$J_{0,rad}$ (A/cm <sup>2</sup> )	$1.77 \times 10^{-15}$	$1.15 \times 10^{-16}$
$V_{oc,rad}$ (mV)	797	864
$J_{sc}$ (mA/cm <sup>2</sup> ) measured	35.18	37.3
$V_{oc}$ (mV) measured	580	679
$\Delta V_{oc,nrad}$ (mV)	217	185
$\Delta V_{oc,nrad}/V_{oc,rad}$	0.27	0.21
Eff (%)	13.8	21

and interfaces, the non-radiative recombination is dominated by Shockley-Read-Hall (SRH) recombination via defect levels in the bandgap of the silicon semiconductor. Otherwise, the surface recombination and Auger

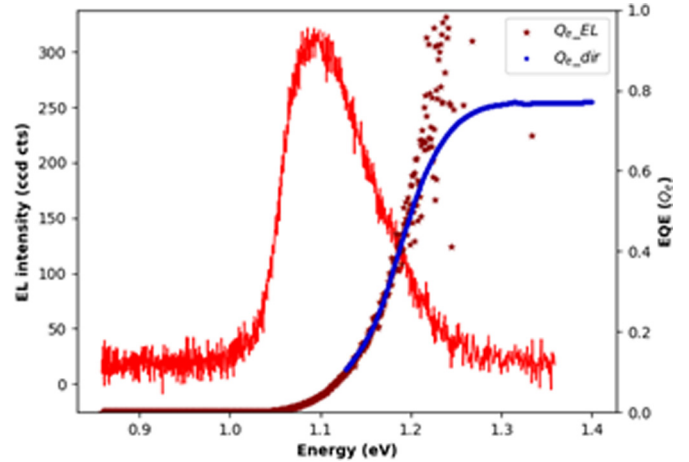


**Fig. 10.** EL spectrum (red line) and measured external quantum efficiency  $Q_{e\_dir}$  (solid circle). Note that EL spectrum corresponds to the  $\varphi_{em}(E)$  in equation (3). Star points represent the calculated quantum efficiencies  $Q_{e\_EL}$  that follow from EL spectrum using equation (3).

recombination are relevant for the silicon solar cells in case of poor passivation and high injection conditions, which the case when the applied bias voltage is 0.9 V corresponding to  $150 \text{ mA/cm}^2$  current density [24,25].

Extensive investigations with other characterization techniques are thus necessary to accurately distinguish the exact nature of these recombination mechanisms that impact the Si-IBC solar cell performance.

## 5 Summary

We have presented application of the electroluminescence technique to characterize silicon interdigitated back contact solar cells for the application as the silicon bottom subcell of a tandem solar cell. Using EL imaging, we have developed a rapid characterization method for two types of cells. First, we have identified the impact of the optical and resistive losses on EL images under different, forward bias voltages. We have also obtained qualitative information on the local variation of the optoelectronic properties of each device. Finally, we have developed an efficiency analysis of the silicon interdigitated cell based on coupled electroluminescence and direct external quantum efficiency spectra. Results show that the interdigitated solar cell has a ratio of non-radiative to radiative recombination equal to 0.27.

This value quantitatively demonstrates a dominance of non-radiative recombination, limiting the open circuit voltage and, therefore, the cell efficiency well below what is achievable with radiatively limited materials.

This work paves the way for an improved manufacturing process for both the interdigitated cell and the upcoming three-terminal tandem cell. Future work can also consider measurement of EL in absolute units, using calibration techniques which have been validated by Tsui et al. [26]. In future work, we will apply electroluminescence analysis to the complete three-terminal perovskite on silicon tandem solar cells

The authors acknowledge the support of the ANR French national agency, which has funded the THESIS project (2019-2024) and the H2020 SOLAR-ERANET program for supporting the BOBTANDEM project, which has contributed to this work.

## Conflict of interest

The authors declare no conflict of interest.

## References

1. K. Wang, M. Silver, D. Han, *J. Appl. Phys.* **73**, 4567 (1993)
2. T. Fuyuki, H. Kondo, T. Yamazaki, Y. Takahashi, Y. Uraoka, *Appl. Phys. Lett.* **86**, 262108 (2005)
3. K. Ramspeck, K. Bothe, D. Hinken, B. Fischer, J. Schmidt, R. Brendel, *Appl. Phys. Lett.* **90**, 153502 (2007)
4. K. Bothe, K. Ramspeck, D. Hinken, R. Brendel, *ECS Trans.* **16**, 63 (2008)
5. A. Bauknecht, S. Siebentritt, J. Albert, M.Ch. Lux-Steiner, *J. Appl. Phys.* **89**, 4391 (2001)
6. T. Trupke, R. A. Bardos, *Appl. Phys. Lett.* **89**, 044107 (2006)
7. P. Würfel, T. Trupke, T. Puzzer, E. Schäffer, W. Warta, S.W. Glunz, *J. Appl. Phys.* **101**, 123110 (2007)
8. J.A. Giesecke, M. Kasemann, W. Warta, *J. Appl. Phys.* **106**, 014907 (2009)
9. O. Breitenstein, A. Khanna, Y. Augarten, J. Bauer, J.-M. Wagner, K. Iwig, *Phys. Status Solidi (RRL)* **4**, 7 (2010)
10. T. Nagashima, K. Okumura, K. Murata, Y. Kimura, in *Conference Record of the Twenty-Eighth IEEE Photovoltaic Specialists Conference – 2000* (Cat. No.00CH37036), pp. 1193–1196 (2000)
11. E. Warren, W. Macmahon, M. Rienäcker, K. Vansant, R. Whitehead, R. Peibst, A. Tamboli, *ACS Energy Lett.* **5**, 1233 (2020)
12. M. Schnabel et al., *Sustain. Energy Fuels* **4**, 549 (2020)
13. M. Rienäcker et al., *Progr. Photovolt.* **27**, 410 (2019)
14. P. Tockhorn et al., *ACS Appl. Energy Mater.* **3**, 1381 (2020)
15. T. Tayagaki et al., *IEEE JPV* **10**, 358 (2019)
16. Z. Djebbour, W. El-Huni, A. Migan Dubois, J.-P. Kleider, *Progr. Photovolt. Res. Appl.* **27**, 306 (2019)
17. J.P. Connolly, K. Ahanogbe, J.-P. Kleider, H.K.J. Alvarez, M. Nazeeruddin, V. Mihailetschi, P. Baranek, M. Vogt, R. Santbergen, O. Isabella, in *37th European Photovoltaic Solar Energy Conference and Exhibition*, 2020, pp. 56–61
18. W. Shockley, H.J. Queisser, *J. Appl. Phys.* **32**, 510 (1961)
19. P.W. Bridgman, *Phys. Rev.* **31**, 101 (1928)
20. U. Rau, *Phys. Rev. B* **76**, 085303 (2007)
21. T. Kirchartz, U. Rau, *Adv. Energy Mater* **8**, 1703385 (2018)
22. N. Puspitosari, C. Longeaud, *Rev. Sci. Instrum.* **88**, 086112 (2017)
23. T. Kirchartz, U. Rau, M. Kurth, J. Mattheis, J.H. Werner, *Thin Solid Films* **515**, 6238 (2007)
24. M.A. Green, *IEEE Trans. Electr. Dev.* **31**, 671 (1984)
25. A. Richter, S.W. Glunz, F. Werner, J. Schmidt, A. Cuevas, *Phys. Rev. B* **86**, 165202 (2012)
26. E. Tsui et al., *J. Appl. Phys.* **80**, 4599 (1996)

**Cite this article as:** Koffi F. Ahanogbe, José Alvarez, Alexandre Jaffré, James P. Connolly, Marie-Estelle Gueunier-Farret, Erwann Fourmond, Seif El-Whibi, Alain Fave, Perrine Carroy, Zakaria Djebbour, Jean-Paul Kleider, Electroluminescence analysis of silicon interdigitated back contact solar cells with a front surface selective band offset barrier, *EPJ Photovoltaics* **13**, 16 (2022)